Geophysical Research Letters

RESEARCH LETTER
10.1029/2019GL085934

Multilayer Observations and Modeling of Thunderstorm-Generated Gravity Waves Over the Midwestern United States

C. J. Heale[1], J. B. Snively[1], A. N. Bhatt[2], L. Hoffmann[3], C. C. Stephan[4], and E. A. Kendall[2]

[1]Center for Space and Atmospheric Research (CSAR), Embry-Riddle Aeronautical University, Daytona Beach, FL, USA, [2]Center for Geospace Studies, SRI International, Menlo Park, CA, USA, [3]Jülich Supercomputing Centre, Forschungszentrum Jülich, Jülich, Germany, [4]Max Planck Institute for Meteorology, Hamburg, Germany

Abstract We present multilayer observations and numerical simulations of gravity waves (GWs) generated by a series of Mesoscale Convective Systems over the midwestern United States. Strong semiconcentric GWs were observed and modeled, which couple from their tropospheric sources to the thermosphere, displaying strong nonlinearity indicated by instability, breaking, and formation of turbulent vortices. GWs in the stratosphere display a large range of horizontal scales from 34–400 km; however, the smaller wavelength waves break rapidly in the mesosphere and lower thermosphere. Larger-scale (≥150 km) waves dominate in the thermosphere and display northwestward propagation at 200–300 km altitude, opposing the mean winds. Despite strong molecular viscosity and thermal conductivity in the thermosphere, steepened wave fronts, which may indicate nonlinearity, is identified in 630 nm airglow imagers. The agreement between model and data suggests new opportunities for data-constrained simulations that span multilayer observables, including mesosphere and lower thermosphere-region airglow not captured for this event.

Key Points:
- Coherent gravity waves were observed above thunderstorms, in the stratosphere by AIRS and thermosphere by MANGO
- Simulations of waves generated by convective sources defined by radar data closely match the observations in scale
- Results indicate that gravity waves may evolve nonlinearly well into the thermosphere and ionosphere

Supporting Information:
- Supporting Information S1
- Movie S1
- Movie S2

Correspondence to:
C. J. Heale,
healec@erau.edu

Citation:
Heale, C. J., Snively, J. B., Bhatt, A. N., Hoffmann, L., Stephan, C. C., & Kendall, E. A. (2019). Multilayer observations and modeling of thunderstorm-generated gravity waves over the Midwestern United States. *Geophysical Research Letters*, *46*, 14,164–14,174. https://doi.org/10.1029/2019GL085934

Received 21 OCT 2019
Accepted 26 NOV 2019
Accepted article online 3 DEC 2019
Published online 6 DEC 2019

1. Introduction

Gravity waves (GWs) and, more generally, acoustic-gravity waves (which include the full spectrum of GWs along with those for which compressibility may be important to their propagation) play an important role in defining the wind, temperature, and circulation of the Earth's atmosphere (Fritts & Alexander, 2003). They represent one of the dominant mechanisms for transporting energy and momentum from the lower atmosphere to the middle and upper atmosphere (e.g., Garcia & Solomon, 1985; Holton, 1982; Holton & Alexander, 2000; Lindzen, 1981). Deep convection, for example, thunderstorms, Mesoscale Convective Complexes, and Mesoscale Convective Systems (MCSs), represents important sources of GWs, especially at tropical and midlatitudes during local summer (Gong et al., 2015; Hoffmann & Alexander, 2010; Perwitasari et al., 2016; Tsuda et al., 2000). Convectively generated GWs contribute to the summer branch of the Brewer-Dobson Circulation (Alexander & Rosenlof, 2003; Stephan et al., 2016) and drive the Quasi-Biennial Oscillation (Alexander & Holton, 1997; Piani et al., 2000), and the Semi-Annual Oscillation (Ern et al., 2015; Garcia et al., 1997). In the mesosphere and lower thermosphere (MLT), convectively generated GWs can be subject to significant breaking leading to secondary wave generation (Horinouchi et al., 2002; Snively & Pasko, 2003; Vincent et al., 2013) and have significant impacts on mean winds and temperature structure (Vadas & Liu, 2013; Vadas et al., 2014).

Observations of GWs generated by convective sources are numerous and are often confirmed by their concentric or semiconcentric patterns in ground-based and satellite imagery (Gong et al., 2015; Hoffmann & Alexander, 2010; Hoffmann et al., 2013; Miller et al., 2015; Perwitasari et al., 2016; Randall et al., 2017; Sentman et al., 2003; Suzuki et al., 2007; Yue et al., 2009). However, single-instrument observations are often confined to a single layer or profile, thus providing limited spatial and temporal coverage of the wave field and its evolution (Kalisch et al., 2016; Trinh et al., 2016). Several studies have leveraged networks of instruments to observe larger fields of view or multiple layers to study the coupling of waves across vertically separated regions of the atmosphere (Azeem et al., 2015; Mundra et al., 2013; Suzuki et al., 2013; Yue et al., 2014; Xu et al., 2015; Wen et al., 2018). However, considerable complementary opportunities remain via numerical modeling, to elucidate the spatial and temporal domains that present observations cannot capture.

There has been a long history of modeling GWs in order to understand their generation mechanisms (Fovell et al., 1992; Lane et al., 2001; Pfister et al., 1993; Pandya & Alexander, 1999; Song et al., 2003), spectra and characteristics (Alexander & Holton, 1997; Beres et al., 2004; Choi & Chun, 2011; Holton & Alexander, 1999; Lane & Moncrieff, 2008; Lane & Sharman, 2008; Piani et al., 2000), and influences of winds on their propagation and effects of the atmospheric structure (Alexander & Holton, 2004; Beres et al., 2002; Vadas et al., 2009; Walterscheid et al., 2001). Convective GWs have been studied using idealized sources (Alexander & Holton, 2004; Snively & Pasko, 2003), cloud-resolving models based upon soundings (Horinouchi et al., 2002; Lane & Moncrieff, 2008; Vincent et al., 2013), full-physics mesoscale models (Costantino et al., 2015), and in general circulation models via parameterization (e.g., Beres et al., 2002, 2004; Richter et al., 2010) and direct simulation (Liu et al., 2014; Stephan et al., 2019a, 2019b). However, high-resolution observations of middle-atmospheric GWs cannot yet be reproduced efficiently in cloud-resolving models, using simple sources initialized from soundings, nor GW-resolving numerical weather prediction and general circulation models. As a simpler strategy, Grimsdell et al. (2010), Stephan and Alexander (2015), and Stephan et al. (2016) used Doppler radar observations of precipitation rates to infer latent heating rates that drive their simulations. This has been shown advantageous in being able to replicate observations at lower computational expense. However, these studies have to date been confined to the stratosphere and below.

In this paper, we present a comprehensive observational and modeling study, from the ground to the thermosphere, of intense MCSs over the midwest United States on the 8 July 2016, the observations of which are described in section 2. The thunderstorm systems are observed by the Next Generation Radar (NEXRAD) network and later modeled using precipitation rate derived latent heat sources. The associated GWs are observed by the Atmosphere Infrared Sounder (AIRS) 4.3 μm band in the stratosphere (30–40 km altitude) (Aumann et al., 2003), in the ground-based Midlatitude Allsky-imaging Network for GeoSpace Observations (MANGO) in the thermosphere (200–300 km altitude) (Mundra et al., 2013), and are simulated from the ground to 250 km altitude.

2. Observations

Strong GWs were observed by AIRS at 08:30 UT and MANGO between 03:50 UT and 07:30 UT on the 8 July 2016 over the midwestern United States. The GWs are assumed to be generated by three separate MCSs, which originate between 00:00 and 02:00 UT over Texas, eastern Colorado, and Kansas. These systems are shown in the NEXRAD reflectivity maps at 04:15 and 05:15 UT in Figure 1a. The three systems last into the evening local time and progress eastward following the winds. The Texas, Colorado, and Kansas systems have approximate diameters of 126, 196, and 271 km, respectively, at 04:15 UT.

Figure 1b shows the 630 nm airglow intensity difference image at 04:15 and 05:15 UT taken by MANGO, which is projected at 250 km altitude. Note that the difference images are created by subtracting two consecutive images with 4 min of exposure with 1 min in-between; thus, the difference image has an effective 10 min cadence. The 630 nm emission (atomic oxygen red line) arises between 200 and 300 km altitude from $O(^1D)$ (Link & Cogger, 1988), resulting from charge exchange and dissociative chemical processes (with O, O^+, O_2, O_2^+, and e^-). The MANGO imager captures evolving strong, apparently steepened wave fronts (suggesting nonlinearity) between 03:50 UT and 07:30 UT that propagate toward the northeast with wavelengths ranging from 200 to 300 km and periods ranging from ~13–45 mins (suggesting phase speeds of 80–106 ms^{-1}) (see supporting information for the MANGO movie).

Figure 1c shows the AIRS 8.1 and 4.3 μm brightness temperature perturbations at 01:30 LT (08:30 UT over Kansas). The 8.1 μm waveband shows the cloud top temperatures where values less than ~200 K are indicative of possible tropopause overshooting. The 4.3 μm waveband peaks at ~30–40 km altitude and is sensitive to GWs with vertical wavelengths greater than ~15 km (Gong et al., 2015; Hoffmann & Alexander, 2010; Hoffmann et al., 2013). The AIRS images show semiconcentric GWs propagating primarily eastward at a range of scales, with smaller scales close to the source and larger scales further away. These range from 34–413 km, with spectral power peaks near 34, 58, 155, 256, and 413 km; however, it is noted that the horizontal resolution is degraded at scan extremes (41 km) versus nadir (13.5 km); thus, smaller scales will not be detected away from nadir. The mean winds in the upper stratosphere are directed almost due west and will filter (via critical levels) westward propagating waves with phase speeds less than ~60 m/s (hence, the lack of westward propagating waves in the image). It is also noted that the AIRS instrument is sensitive to

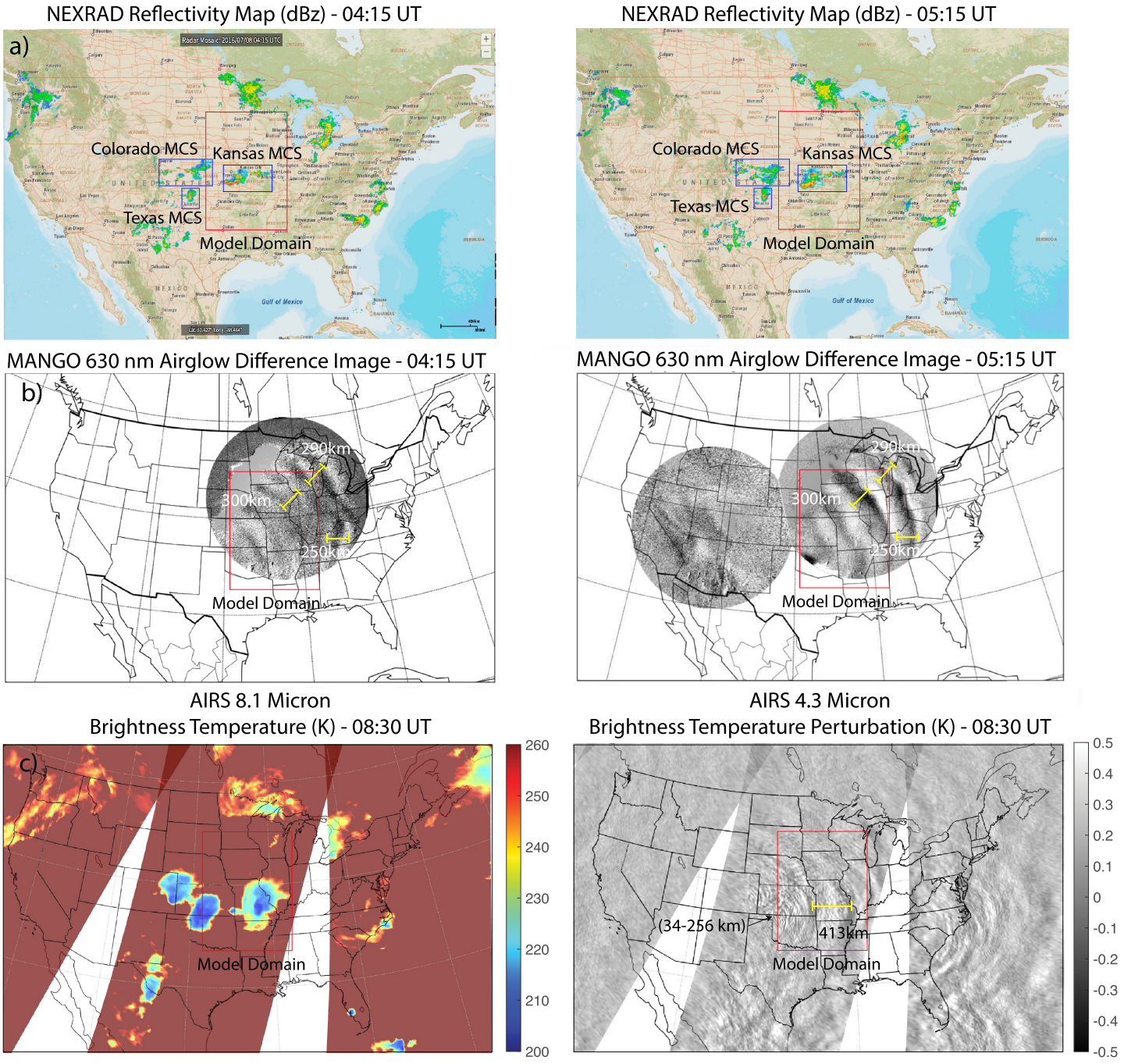

Figure 1. The (a) NEXRAD reflectivity map at 04:15 and 05:15 UT with three major storm systems in blue boxes, (b) the MANGO 630 nm difference image at 04:15 and 05:15 UT, and (c) the AIRS 8.1 and 4.3 μm brightness temperature perturbations at 08:30 UT over Kansas. The red box shows the model simulation domain. Yellow bars indicate wave scales.

waves with larger vertical wavelengths (Hoffmann & Alexander, 2009). Waves that are propagating in the direction of the wind will be refracted to smaller vertical wavelength and will have small perturbations in the AIRS image as a result.

The times at which the data are displayed in Figure 1 are subject to constraints of data availability. AIRS passes a given location twice a day (01:30 LT and 13:30 LT); thus, only one nighttime observation is available for this event. The MANGO observation is displayed at 04:15 and 05:15 UT due to the coherence of the waves at this time and its evolution into a steepened waveform. The NEXRAD data are shown at the same

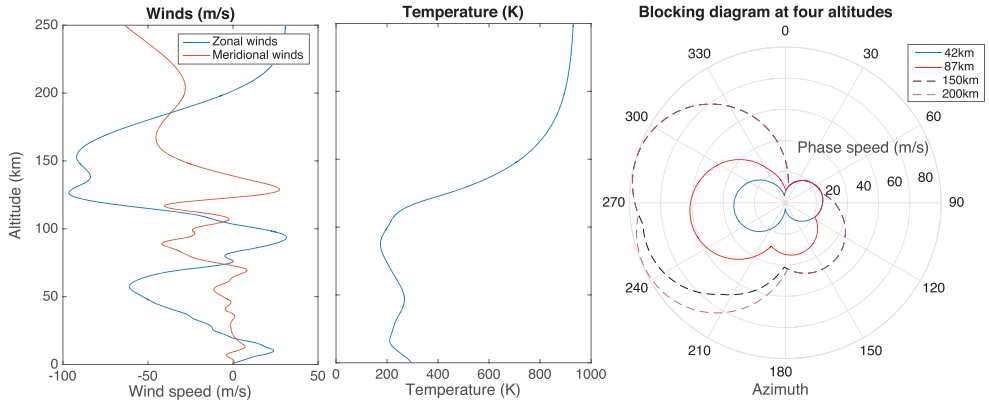

Figure 2. The (left) ambient zonal and meridional winds, (middle) temperature structure, and (right) blocking diagram at $z = 42$, 87, 150, and 200 km altitude. The blocking diagram line contours shows the range of phase speeds which are critical level filtered, along a given azimuth, below a given altitude.

time for comparison. Since waves pass through the stratosphere before they reach thermosphere, it would to be preferable to have either MANGO and AIRS data that overlap in time or AIRS data that occurs before the MANGO data, and then the AIRS and MANGO data could be shown at a times which correspond to propagation times between the two layers.

3. Numerical Modeling

The MCS that originates over Kansas, and subsequent GW generation and propagation, is simulated using the 3-D nonlinear, high-resolution, compressible numerical "MAGIC" Model for Acoustic-Gravity wave Interactions and Coupling (Snively & Pasko, 2008; Snively, 2013; Zettergren & Snively, 2015). While there are three major storms systems present in the NEXRAD data over the observation period, the Kansas is the most prominent and has the most intense rainfall. The other two major storm system originate outside of the extent of the model domain and will be included in a future more comprehensive study. The thunderstorm forcing is approximated as a latent heating, derived from NEXRAD digital precipitation rates, and applied to the Navier-Stokes energy equation. The Stephan and Alexander (2015) algorithm takes the precipitation rate (in units of mm/10 min) as input and outputs a latent heating profile for each x, y, and t using a minimum convective threshold of 1 mm/10 min. The algorithm is a simple linear regression derived from precipitation rates and heating profiles within a full-physics version of the Weather Forecasting Model at 4×4 m resolution and was validated against a number of real storms and satellite data. The regression lines use the precipitation rate as the independent variable and the dependent variables are top, center, and bottom of heating/cooling profile and heating/cooling amplitude. The MAGIC domain used in this simulation is $1{,}200 \times 1{,}200 \times 250$ km (x, y, and z), with resolutions of $2 \times 2 \times 1$ km, respectively. The side and top boundaries are open (a sponge layer is applied to the top 30 km of the domain), and the bottom boundary is reflective. The model domain is indicated via the red box in Figure 1, and only thunderstorms which are present within this domain are modeled. Therefore, we consider only a subset of sources that can generate GWs that may be present in the image data sets.

3.1. Ambient Atmosphere

The ambient atmosphere used for the simulation consisted of Modern-Era Retrospective analysis for Research and Applications, Version 2 (Gelaro et al., 2017) for the winds between $z = 0$–60 km altitude, and the Horizontal Wind Model 2007 (Drob et al., 2008) between $z = 60$–250 km. The background species density and temperature profiles are generated using the 2001 U.S. Naval Research Laboratory Mass Spectrometer and Incoherent Scatter Radar Exosphere (NRLMSISE-00) (Picone et al., 2002). The profiles were chosen at a latitude of 38° N and a longitude of 267° E (corresponding to the location of the Kansas thunderstorm) at 6:00 UT on 8 July 2016 and are homogeneous in latitude, longitude, and time. The profiles are displayed in Figure 2, along with a "blocking diagram" to depict phase speeds that would be cumulatively filtered by critical levels, as a function of azimuth at four different altitudes (42, 87, 150, and 200 km). For example, the blue/red/black contour line indicates the minimum phase speed needed for a wave to propagate up to

42/87/150 km altitude, respectively, and avoid being critical level filtered, along a given azimuth. Alternatively stated, all waves with phase speeds that fall within the contour will be critical level filtered before reaching the respective altitude. Figure 2c suggests significant blocking occurs for westward propagating GWs; those propagating along a northeastern trajectory are least likely to be filtered by critical levels.

3.2. Simulation Results

The MAGIC model output data enable calculation of synthetic AIRS 4.3 μm images following the techniques of Grimsdell et al. (2010) and Stephan and Alexander (2015). It also supports OH and OI airglow chemistry (e.g., Snively et al., 2010, and references therein), calculated time dependently, with the ability to output volume emission rate or brightness temperature perturbation "images" or "Keograms," for comparison with airglow imaging data at 87 and 95 km altitude, respectively. Note that direct comparison with the 630 nm MANGO data will require the use of a comprehensive ionospheric model; this will be performed and reported later.

Figure 3 shows synthetic AIRS (stratosphere), OH(3,1) airglow (mesosphere), and $z = 150$ km (thermosphere) temperature perturbations at $t = 2$, 3, and 4 UT. The AIRS results mimic the observations, finding a range of scales that increase at greater distances from the source and showing predominately eastward propagation; the amplitudes are of the same order as the observations. There are two sources of GWs that are distinct at 02:00 and 03:00 UT; however, the fronts are superposed by 04:00 UT. The simulated AIRS signatures appear linear at this altitude. This is deduced because the wavefields are relatively sinusoidal, have small amplitudes, and display no evidence of instability within the limits of their resolution. The dominant horizontal wavelength is 40 km, and the period is 11.7 min ($C_p = 56$ m/s), compared with 34 km in the observation.

The OH(3,1) temperature perturbation fields (Figure 3b, centered at $z = 87$ km) shows rapid breaking of GWs propagating in the eastward direction, destroying the wave field and leaving the larger-scale (higher phase speed) waves to become dominant by 04:00 UT. This is predominantly due to the large zonal shear in the MLT (which reduces the GW vertical wavelength and Richardson number) and the large amplitudes that the GWs attain. In the meridional direction, breaking is less prevalent since the wind shear (and amplitude) is not as strong. Therefore, the dominant-scale sizes propagating meridionally are smaller than those propagating zonally. The dominant zonally propagating waves are 170 and 200 km in scale with 27 and 50 min periods, respectively (66–105 m/s phase speed), and the meridional waves have dominant-scale sizes and periods of 100 km and 21.8 min, respectively ($C_p = 76$ m/s). The smaller-scale (~34–60 km), slower phase speed waves that are dominant in the stratosphere are those that tend to break in the mesosphere.

The temperature perturbation field in the thermosphere at $z = 150$ km is shown in Figure 3c. Molecular viscosity and thermal conductivity are significant at these altitudes, and the waves should experience significant damping. Despite this, the GW field still displays strong nonlinearity, breaking, and generation of vortices at ~tens of km scales. This supports the MANGO results that display possible steepened wave features, suggesting nonlinearity, where wave damping is significant. The waves propagate predominately eastward with a dominant scale of 170 km and a 29 min period and a strong secondary mode with 75 km scale and a 13.8 min period (phase speeds of 97 and 90 m/s, respectively). The eddy scales are much larger at 150 km than those in the OH(3,1) at 87 km, due to the higher viscosity at 150 km precluding the evolution to smaller scales. The dominant wave scales and periods correspond to those in the OH(3,1), suggesting that this is the same primary wave packet that propagates all the way up from the source (i.e., it is not the result of wave breaking and secondary wave generation). This mode is also identified in the stratosphere but at much weaker amplitude.

During the model evolution, acoustic oscillations are detectable in the simulated OH(3,1) layer perturbations and the 150 km temperature (e.g., Snively, 2013; Zettergren & Snively, 2013). The acoustic waves clearly exhibit nonlinearity at 150 km, due to nonlinear evolution following amplification as they propagate upward through decreasing density, seen in the video provided as supporting information in frames after 2.25 UT. Examination of global positioning system ionospheric total electron content, following personal communications with Pavel Inchin, identified acoustic waves that are approximately timed with the occurrence of strong acoustic waves in the simulation. This is consistent with prior reports during severe weather (e.g., Nishioka et al., 2013). We caution that the amplitudes of simulated acoustic waves may be in excess of those in reality, due to limitations on source resolution leading to more coherent source regions. This will be investigated in future modeling, with ionospheric responses.

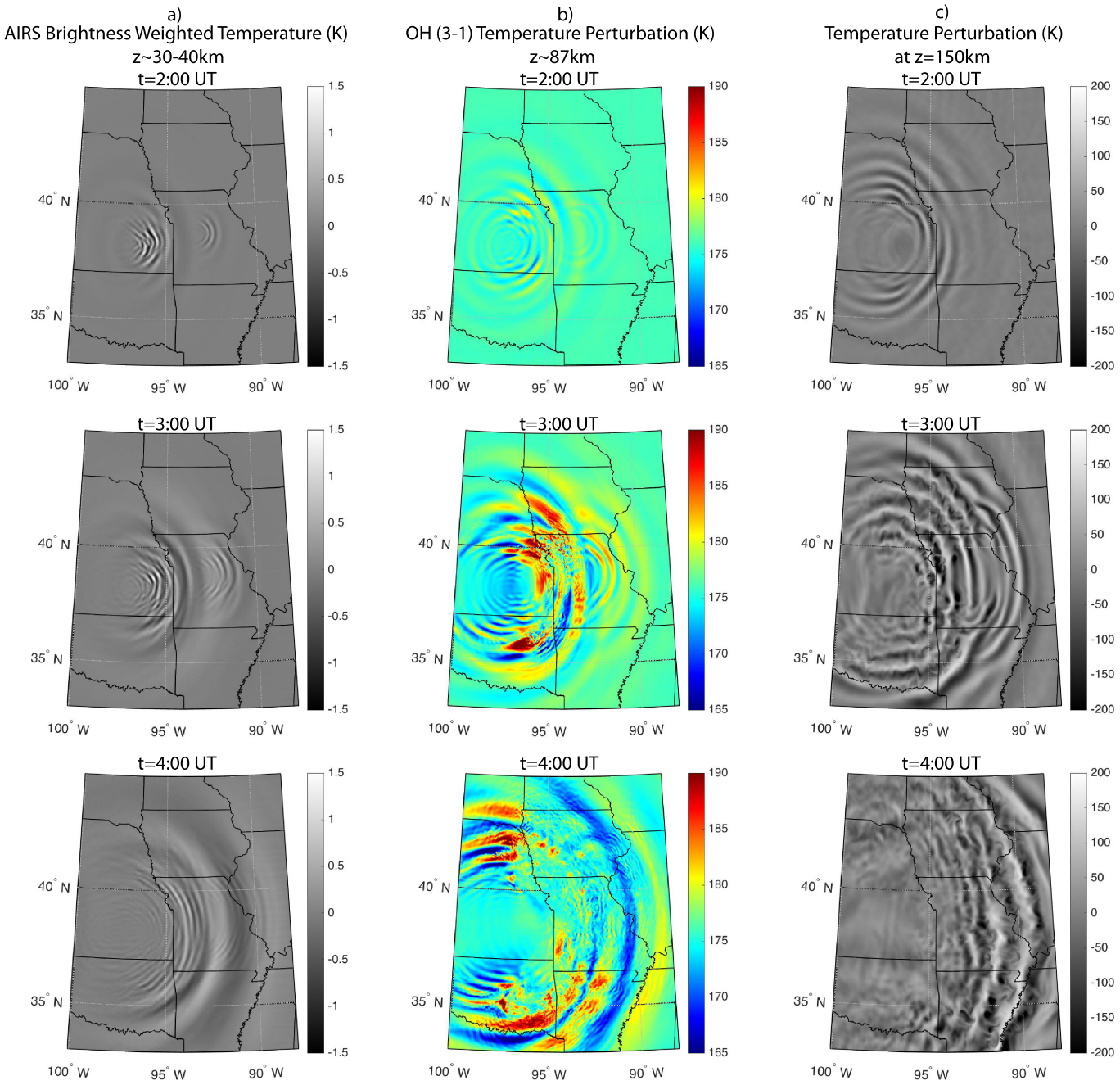

Figure 3. The simulated (a) AIRS brightness temperature perturbations, (b) OH(3,1) temperature emission, and (c) $z = 150$ km model temperature perturbation at $t = 02{:}00$, 03:00, and 04:00 UT.

4. Comparison of Observations and Simulated Results

Figure 4 shows a comparison of the stratospheric and thermospheric observation data and simulation results at single times. The synthetic AIRS data, temperature perturbation at 150 km, and the MANGO data are all displayed at approximately the same time (~4:15 UT). The AIRS imagery, however, was captured later at 08:30 UT, which is beyond the duration of the present simulation; separate simulation results at lower resolution, not shown here, show persistence of these stratospheric wave fields to at least 08:00 UT, in reasonable agreement with AIRS.

For analysis, a single slice of the AIRS (and synthetic AIRS) data was taken along the red line for each case, and a Morlet wavelet transform was performed along that red line using the method of Torrence and

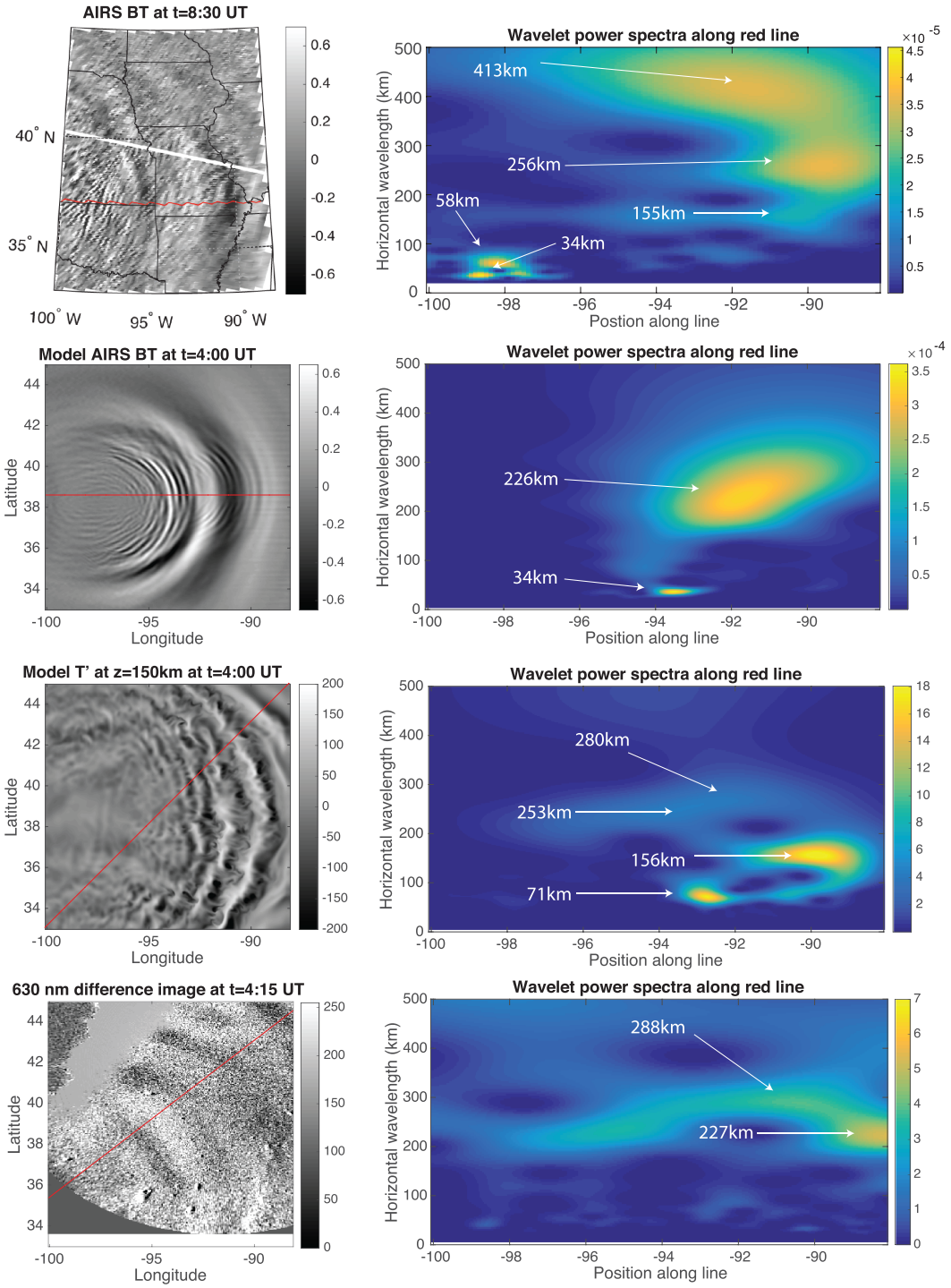

Figure 4. A comparison of the model and the observations at fixed times (left), along with corresponding wavelet transforms (right). The top row shows the AIRS brightness temperature perturbation at 8:30 UT, the second row shows the simulated AIRS brightness temperature at 4:00 UT, the third row shows the simulated temperature perturbation at z = 150 km, at 4:00 UT, and the bottom row shows the MANGO data at 4:15 UT.

Compo (1998). The slice was taken zonally in the stratosphere and in the northeast direction in the thermosphere. The slices are taken so that they align with the dominant wave propagation direction at each altitude. Despite the AIRS data being collected at a different time than our simulation results, the model captures the prominent 34 km small-scale and 155–290 km modes but does not capture a distinct 56 km mode or the 413 km large-scale mode. This may be due to the difference in timing and sources included in the model versus those that are represented in the data. In the thermosphere, the model results at 150 km altitude suggest a wave that is propagating zonally with dominant modes at 71 km, 156 km, and a broad, weaker mode ranging from around 200–300 km.

The MANGO data also show a distinctly northeastward propagating GW with scales between 220 and 290 km. These scales are similar to the broad, weaker modes seen in the simulation. However, there was a large MCS in Texas (southwest of the observation), which fell outside of the model domain and may play a role in the distinct northeastward propagating waves and scales observed. In addition, the MANGO data are the result of an emission layer which spans 200–300 km and is complicated by integrated averaging and line-of-sight cancelation effects; as well, the ionospheric responses depend on the state of the ionosphere and the local geometry of the geomagnetic field. Most notably, ionospheric responses should be stronger for northward waves than eastward waves, which may further enhance the observable anisotropy in a manner consistent with these data (e.g., Nishioka et al., 2013; Zettergren & Snively, 2013).

5. Discussion and Conclusions

This paper presents a multilayer study of GWs generated by convective systems over the midwestern United States on 8 July 2016. Three MCSs, originating over Colorado, Texas, and Kansas, were present throughout the day and generated significant wave activity observed by the AIRS instrument in the stratosphere and by a MANGO 630 nm airglow camera (situated in Iowa) in the thermosphere. Complementary modeling was performed, where GWs were forced by time-dependent latent heating sources representative of the MCSs, to provide synthetic AIRS and OH(3,1) images, as well as the temperature perturbation in the thermosphere at $z = 150$ km to assess the waves exiting the MLT into the thermosphere.

The GWs propagated predominately toward the east, due to filtering by the strong westward stratospheric winds, displaying an arc-like morphology. Interference is seen between waves generated by different individual convective plumes within the MCSs, revealing a broad range of scales. The GW horizontal scales in AIRS ranged from 34–413 km. Similar scales were found in the simulation with a dominant mode of 40 km and a period of 11.7 min. Rapid breaking occurred for the eastward propagating waves in the OH(3,1) simulated images due to a large zonal shear in the MLT; the smaller scales that were dominant in the stratosphere break up into smaller structures, and larger scale ≥150 km GWs remain to dominate the spectrum. In contrast, smaller-scale GWs avoid breaking in the meridional direction, due to a lack of strong wind shear, and thus persist. The same larger ≥150 km waves become dominant in the thermosphere at 150 km altitude. These waves exhibit large amplitude, nonlinearity, and instability at these altitudes, leading to relatively larger-scale secondary structures than in the MLT due to the greater effects of molecular viscosity. The waves observed in the 630 nm airglow images propagate to the northeast, against the mean wind over the 150–200 km altitude region.

This study further highlights the importance of multilayer observations and modeling to investigate wave coupling throughout the atmosphere. Here, GWs with scales between 155 and 290 km are present at all observed altitudes and indicate primary wave coupling from the source to the thermosphere at considerable amplitudes. Above mesopause, they have typical phase speeds of ~90–110 m/s. Furthermore, despite the fact that most GWs are assumed to be heavily damped in the thermosphere by viscosity, these GWs still exhibit steepening and breaking in the model as they reach 150 km altitude. This interpretation is further supported by the MANGO 630 nm difference images, which also provide compelling observational evidence for the importance of nonlinearity.

We consider these results to be extremely encouraging and are developing further numerical experiments to investigate this event in greater detail, albeit at much greater computational cost. Thus, we are now performing larger-domain, higher-resolution case studies, over the full duration of the event extending to the time of the AIRS observation. This case study will also incorporate other nearby sources and will extend throughout the thermosphere to enable direct calculation of the ionospheric responses leading to signatures in 630 nm airglow and vertically integrated total electron content (e.g., Zettergren & Snively, 2015),

for the full relevant spectrum of AGW-GW. These studies form a crucial step toward understanding the impacts of waves that are unresolved in large-scale models and provide specific demonstration of the feasibility to include upper-atmospheric responses in deep-atmosphere mesoscale models using simplified, data-constrained sources. This is the first study that looks at multilayer dynamics from diverse observational sources and simulations, which gives unprecedented insight into the regional processes that enable momentum transfer via GWs

Acknowledgments
C. J. Heale and J. B. Snively were supported under NASA Grant 80NSSC18K1037 to Embry-Riddle. AIRS data were obtained online (http://doi.org/10.17616/R34J42). C. C. Stephan was supported by the Minerva Fast Track Program of the Max Planck Society. MANGO data are available online (http://mango.sri.com/). MANGO was supported by NSF Grant AGS-1452357. MANGO investigators are grateful to the Eastern Iowa Observatory for hosting the imager used in this study. NEXRAD data were obtained online (https://www.ncdc.noaa.gov/data-access/radar-data/nexrad). MERRA-2 data can be accessed online (https://gmao.gsfc.nasa.gov/reanalysis/MERRA-2/data_access/). We gratefully acknowledge use of the ERAU Vega High-Performance Computing Cluster in completing these simulations. We are grateful for discussions with P. Inchin. The simulation data shown are too voluminous to retain (many terabytes) and are theoretical in nature; thus, detailed movies of simulation results are provided instead as supporting information to enable quantitative reproducibility.

References

Alexander, M. J., & Holton, J. R. (1997). A model study of zonal forcing in the equatorial stratosphere by convectively induced gravity waves. *Journal of the Atmospheric Sciences*, *54*, 408–419. https://doi.org/10.1175/1520-0469(1997)054<0408:AMSOZF>2.0.CO;2

Alexander, M. J., & Holton, J. R. (2004). On the spectrum of vertically propagating gravity waves generated by a transient heat source. *Atmospheric Chemistry and Physics*, *4*, 923–932. https://doi.org/10.5194/acp-4-923-2004

Alexander, M. J., & Rosenlof, K. H. (2003). Gravity-wave forcing in the stratosphere: Observational constraints from the upper atmosphere research satellite and implications for parameterization in global models. *Journal of Geophysical Research*, *108*(D19), 4597. https://doi.org/10.1029/2003JD003373

Aumann, H. H., Chahine, M. T., Gautier, C., Goldberg, M. D., Kalnay, E., McMillin, L. M., & Susskind, J. (2003). AIRS/AMSU/HSB on the Aqua mission: Design, science objectives, data products, and processing systems. *IEEE Transactions on Geoscience and Remote Sensing*, *41*(2), 253–264.

Azeem, I., Yue, J., Hoffmann, L., Miller, S. D., Straka, W. C. III, & Crowley, G. (2015). Multisensor profiling of a concentric gravity wave event propagating from the troposphere to the ionosphere. *Geophysical Research Letters*, *42*, 7874–7880. https://doi.org/10.1002/2015GL065903

Beres, J. H., Alexander, M. J., & Holton, J. R. (2002). Effects of tropospheric wind shear on the spectrum of convectively generated gravity waves. *Journal of the Atmospheric Sciences*, *59*(11), 1805–1824.

Beres, J. H., Alexander, M. J., & Holton, J. R. (2004). A method of specifying the gravity wave spectrum above convection based on latent heating properties and background wind. *Journal of the Atmospheric Sciences*, *61*(3), 324–337.

Choi, H. J., & Chun, H. Y. (2011). Momentum flux spectrum of convective gravity waves. Part I: An update of a parameterization using mesoscale simulations. *Journal of the Atmospheric Sciences*, *68*(4), 739–759. https://doi.org/10.1175/2010JAS3552.1

Costantino, L., Heinrich, P., Mzé, N., & Hauchecorne, A. (2015). Convective gravity wave propagation and breaking in the stratosphere: Comparison between WRF model simulations and lidar data. *Annales Geophysicae*, *33*(9), 1155–1171. https://doi.org/10.5194/angeo-33-1155-2015

Drob, D. P., Emmert, J. T., Crowley, G., Picone, J. M., Shepherd, G. G., Skinner, W., & Vincent, R. A. (2008). An empirical model of the Earth's horizontal wind fields: HWM07. *Journal of Geophysical Research*, *113*, A12304. https://doi.org/10.1029/2008JA013668

Ern, M., Preusse, P., & Riese, M. (2015). Driving of the SAO by gravity waves as observed from satellite. *Annales Geophysicae*, *33*(4), 483–504. https://doi.org/10.5194/angeo-33-483-2015

Fovell, R., Durran, D., & Holton, J. R. (1992). Numerical simulations of convectively generated stratospheric gravity waves. *Journal of the Atmospheric Sciences*, *49*, 1427–1442.

Fritts, D., & Alexander, M. J. (2003). Gravity wave dynamics and effects in the middle atmosphere. *Reviews of Geophysics*, *41*(1), 1003. https://doi.org/10.1029/2001RG000106

Garcia, R. R., Dunkerton, T. J., Lieberman, R. S., & Vincent, R. A. (1997). Climatology of the semiannual oscillation of the tropical middle atmosphere. *Journal of Geophysical Research*, *102*(D22), 26,019–26,032. https://doi.org/10.1029/97JD00207

Garcia, R. R., & Solomon, S. (1985). The effect of breaking gravity waves on the dynamics and chemical composition of the mesosphere and lower thermosphere. *Journal of Geophysical Research*, *90*, 3850–3868.

Gelaro, R., McCarty, W., Suárez, M. J., Todling, R., Molod, A., Takacs, L., & Zhao, B. (2017). The Modern-Era Retrospective Analysis for Research and Applications, Version 2 (MERRA-2). *Journal of Climate*, *30*(14), 5419–5454. https://doi.org/10.1175/JCLI-D-16-0758.1

Gong, J., Yue, J., & Wu, D. L. (2015). Global survey of concentric gravity waves in AIRS images and ECMWF analysis. *Journal of Geophysical Research: Atmospheres*, *120*, 2210–2228. https://doi.org/10.1002/2014JD022527

Grimsdell, A. W., Alexander, M. J., May, P. T., & Hoffmann, L. (2010). Model study of waves generated by convection with direct validation via satellite. *Journal of the Atmospheric Sciences*, *67*(5), 1617–1631. https://doi.org/10.1175/2009JAS3197.1

Hoffmann, L., & Alexander, M. J. (2009). Retrieval of stratospheric temperatures from Atmospheric Infrared Sounder radiance measurements for gravity wave studies. *Journal of Geophysical Research*, *114*, D07105. https://doi.org/10.1029/2008JD011241

Hoffmann, L., & Alexander, M. J. (2010). Occurrence frequency of convective gravity waves during the North American thunderstorm season. *Journal of Geophysical Research*, *115*, D20111. https://doi.org/10.1029/2010JD014401

Hoffmann, L., Xue, X., & Alexander, M. J. (2013). A global view of stratospheric gravity wave hotspots located with Atmospheric Infrared Sounder observations. *Journal of Geophysical Research: Atmospheres*, *118*, 416–434. https://doi.org/10.1029/2012JD018658

Holton, J. R. (1982). The role of gravity wave induced drag and diffusion in the momentum budget of the mesosphere. *Journal of the Atmospheric Sciences*, *39*, 791–799.

Holton, J. R., & Alexander, M. J. (1999). Gravity waves in the mesosphere generated by tropospheric convention. *Tellus B*, *51*(1), 45–58. https://doi.org/10.1034/j.1600-0889.1999.00005.x

Holton, J. R., & Alexander, M. J. (2000). The role of waves in the transport circulation of the middle atmosphere. In D. E. Siskind, S. L. Ekermann, & M. E. Summers (Ed.), *Atmospheric science across the stratopause* (pp. 21–35). American Geophysical Union.

Horinouchi, T., Nakamura, T., & Kosaka, J. i. (2002). Convectively generated mesoscale gravity waves simulated throughout the middle atmosphere. *Geophysical Research Letters*, *29*(21), 2007. https://doi.org/10.1029/2002GL016069

Kalisch, S., Chun, H. Y., Ern, M., Preusse, P., Trinh, Q. T., Eckermann, S. D., & Riese, M. (2016). Comparison of simulated and observed convective gravity waves. *Journal of Geophysical Research: Atmospheres*, *121*, 13,474–13,492. https://doi.org/10.1002/2016JD025235

Lane, T. P., & Moncrieff, M. W. (2008). Stratospheric gravity waves generated by multiscale tropical convection. *Journal of the Atmospheric Sciences*, *65*(8), 2598–2614. https://doi.org/10.1175/2007JAS2601.1

Lane, T. P., Reeder, M. J., & Clark, T. L. (2001). Numerical modeling of gravity wave generation by deep tropical convection. *Journal of the Atmospheric Sciences*, *58*, 1249–1274.

Lane, T. P., & Sharman, R. D. (2008). Some influences of background flow conditions on the generation of turbulence due to gravity wave breaking above deep convection. *Journal of Applied Meteorology and Climatology*, *11*, 2777–2796. https://doi.org/10.1175/2008JAMC1787.1

Lindzen, R. S. (1981). Turbulence and stress owing gravity wave and tidal breakdown. *Journal of Geophysical Research*, *86*(C10), 9707–9714.

Link, R., & Cogger, L. L. (1988). A reexamination of the OI 6300-Å nightglow. *Journal of Geophysical Research*, *93*, 9883–9892.

Liu, H. L., McInerney, J. M., Santos, S., Lauritzen, P. H., Taylor, M. A., & Pedatella, N. M. (2014). Gravity waves simulated by high-resolution Whole Atmosphere Community Climate Model. *Geophysical Research Letters*, *41*, 9106–9112. https://doi.org/10.1002/2014GL062468

Miller, S. D., Straka, W. C., Yue, J., Smith, S. M., Alexander, M. J., Hoffmann, L., & Partain, P. T. (2015). Upper atmospheric gravity wave details revealed in nightglow satellite imagery. *Proceedings of the National Academy of Sciences*, *112*(49), E6728–E6735. https://doi.org/10.1073/pnas.1508084112

Mundra, R., Kengne, F., & Rangel, A. (2013). Mid-latitude all-sky-imager network for geophysical observation. https://doi.org/10.13140/2.1.1789.7762

Nishioka, M., Tsugawa, T., Kubota, M., & Ishii, M. (2013). Concentric waves and short-period oscillations observed in the ionosphere after the 2013 Moore EF5 tornado. *Geophysical Research Letters*, *40*, 5581–5586. https://doi.org/10.1002/2013GL057963

Pandya, R. E., & Alexander, M. J. (1999). Linear stratospheric gravity waves above convective thermal forcing. *Journal of the Atmospheric Sciences*, *56*, 2434–2446.

Perwitasari, S., Sakanoi, T., Nakamura, T., Ejiri, M. K., Tsutsumi, M., Tomikawa, Y., & Saito, A. (2016). Three years of concentric gravity wave variability in the mesopause as observed by IMAP/VISI. *Geophysical Research Letters*, *43*, 11,528–11,535. https://doi.org/10.1002/2016GL071511

Pfister, L., Chan, K. R., Bui, T. P., Bowen, S., Legg, M., Gary, B., & Starr, W. (1993). Gravity waves generated by a tropical cyclone during the STEP tropical field program: A case study. *Journal of Geophysical Research*, *98*, 8611–8638.

Piani, C., Durran, D., Alexander, M. J., & Holton, J. R. (2000). A numerical study of three-dimensional gravity waves triggered by deep tropical convection and their role in the dynamics of the QBO. *Journal of the Atmospheric Sciences*, *57*, 3689–3702.

Picone, J. M., Hedin, A. E., Drob, D. P., & Aikin, A. (2002). NRL-MSISE-00 Empirical Model of the Atmosphere: Statisical comparisons and scientific issues. *Journal of Geophysical Research*, *107*(A12), 1468. https://doi.org/10.1029/2002JA009430

Randall, C. E., Carstens, J., France, J. A., Harvey, V. L., Hoffmann, L., Bailey, S. M., & Russell, J. M. (2017). New AIM/CIPS global observations of gravity waves near 50-55 km. *Geophysical Research Letters*, *44*, 7044–7052. https://doi.org/10.1002/2017GL073943

Richter, J. H., Sassi, F., & Garcia, R. R. (2010). Towards a physically based gravity waves source parameterization in a general circulation model. *Journal of the Atmospheric Sciences*, *67*, 136–156.

Sentman, D., Wescott, E., Picard, R., Winick, J., Stenbaek-Nielsen, H., Dewan, E., & Morrill, J. (2003). Simultaneous observations of mesospheric gravity waves and sprites generated by a midwestern thunderstorm. *Journal of Atmospheric and Solar-Terrestrial Physics*, *65*, 537–550.

Snively, J. B. (2013). Mesospheric hydroxyl airglow signatures of acoustic and gravity waves generated by transient tropospheric forcing. *Geophysical Research Letters*, *40*, 4533–4537. https://doi.org/10.1002/grl.50886

Snively, J. B., & Pasko, V. P. (2003). Breaking of thunderstorm-generated gravity waves as a source of short-period ducted waves at mesopause altitudes. *Geophysical Research Letters*, *30*(24), 2254. https://doi.org/10.1029/2003GL018436

Snively, J. B., & Pasko, V. P. (2008). Excitation of ducted gravity waves in the lower thermosphere by tropospheric sources. *Journal of Geophysical Research*, *113*, A06303. https://doi.org/10.1029/2007JA012693

Snively, J. B., Pasko, V. P., & Taylor, M. J. (2010). OH and OI airglow layer modulation by ducted short-period gravity waves: Effects of trapping altitude. *Journal of Geophysical Research*, *115*, A11311. https://doi.org/10.1029/2009JA015236

Song, I., Chun, H. Y., & Lane, T. P. (2003). Generation mechanisms of convectively forced internal gravity waves and their propagation to the stratosphere. *Journal of the Atmospheric Sciences*, *60*, 1960–1980.

Stephan, C. C., & Alexander, M. J. (2015). Realistic simulations of atmospheric gravity waves over the continental U.S. using precipitation radar data. *Journal of Advances in Modeling Earth Systems*, *7*, 823–835. https://doi.org/10.1002/2014MS000396

Stephan, C., Alexander, M. J., & Richter, J. H. (2016). Characteristics of gravity waves from convection and implications for their parameterization in global circulation models. *Journal of the Atmospheric Sciences*, *73*, 2729–2742.

Stephan, C., Strube, C., Klocke, D., Ern, M., Hoffmann, L., Preusse, P., & Schmidt, H. (2019a). Intercomparison of gravity waves in global convection-permitting models. *Journal of the Atmospheric Sciences*, *76*, 2739–2759. https://doi.org/10.1175/JAS-D-19-0040.1

Stephan, C. C., Strube, C., Klocke, D., Ern, M., Hoffmann, L., Preusse, P., & Schmidt, H. (2019b). Gravity waves in global high-resolution simulations with explicit and parameterized convection. *Journal of Geophysical Research: Atmospheres*, *124*, 4446–4459. https://doi.org/10.1029/2018JD030073

Suzuki, S., Shiokawa, K., Otsuka, Y., Ogawa, T., Nakamura, K., & Nakamura, T. (2007). A concentric gravity wave structure in the mesospheric airglow images. *Journal of Geophysical Research*, *112*, D02102. https://doi.org/10.1029/2005JD006558

Suzuki, S., Vadas, S. L., Shiokawa, K., Otsuka, Y., Karwamura, S., & Murayama, Y. (2013). Typoon-induced concentric airglow structures in the mesopause region. *Geophysical Research Letters*, *40*, 5983–5987. https://doi.org/10.1002/2013GL058087

Torrence, C., & Compo, G. P. (1998). A practical guide to wavelet analysis. *Bulletin of the American Meteorological society*, *79*(1), 61–78.

Trinh, Q. T., Kalisch, S., Preusse, P., Ern, M., Chun, H. Y., Eckermann, S. D., & Riese, M. (2016). Tuning of a convective gravity wave source scheme based on HIRDLS observations. *Atmospheric Chemistry and Physics*, *16*(11), 7335–7356. https://doi.org/10.5194/acp-16-7335-2016

Tsuda, T., Nishida, M., Rocken, C., & Ware, R. H. (2000). A global morphology of gravity wave activity in the stratosphere revealed by the GPS occultation data (GPS/MET). *Journal of Geophysical Research*, *105*(D6), 7257–7273. https://doi.org/10.1029/1999JD901005

Vadas, S. L., & Liu, H. L. (2013). Numerical modeling of the large-scale neutral and plasma responses to the body forces created by the dissipation of gravity waves from 6 h of deep convection in Brazil. *Journal of Geophysical Research: Space Physics*, *118*, 2593–2617. https://doi.org/10.1002/jgra.50249

Vadas, S. L., Liu, H. L., & Lieberman, R. S. (2014). Numerical modeling of the global changes to the thermosphere and ionosphere from the dissipation of gravity waves from deep convection. *Journal of Geophysical Research: Space Physics*, *119*, 7762–7793. https://doi.org/10.1002/2014JA020280

Vadas, S. L., Yue, J., She, C. Y., Stamus, P. A., & Liu, A. Z. (2009). A model study of the effects of winds on concentric rings of gravity waves from a convective plume near Fort Collins on 11 May 2004. *Journal of Geophysical Research*, *114*, D06103. https://doi.org/10.1029/2008JD010753

Vincent, R. A., Alexander, M. J., Dolman, B. K., MacKinnon, A. D., May, P. T., Kovalam, S., & Reid, I. M. (2013). Gravity wave generation by convection and momentum deposition in the mesosphere-lower thermosphere. *Journal of Geophysical Research: Atmospheres*, *118*, 6233–6245. https://doi.org/10.1002/jgrd.50372

Walterscheid, R., Schubert, G., & Brinkman, D. (2001). Small-scale gravity waves in the upper mesosphere and lower thermosphere generated by deep tropical convection. *Journal of Geophysical Research*, *106*(D23), 31,825–31,832.

Wen, Y., Zhang, Q., Gao, H., Xu, J., & Li, Q. (2018). A case study of the stratospheric and mesospheric concentric gravity waves excited by thunderstorm in Northern China. *Atmosphere*, *9*, 489.

Xu, J., Li, Q., Yue, J., Hoffmann, L., Straka, W. C. III, Wang, C., & Ning, B. (2015). Concentric gravity waves over northern China observed by an airglow imager network and satellites. *Journal of Geophysical Research: Atmospheres*, *120*, 11,058–11,078. https://doi.org/10.1002/2015JD023786

Yue, J., Miller, S. D., Hoffmann, L., & Straka, W. C. (2014). Stratospheric and mesospheric concentric gravity waves over Tropical Cyclone Mahasen: Joint AIRS and VIIRS satellite observations. *Journal of Atmospheric and Solar-Terrestrial Physics*, *119*, 83–90. https://doi.org/https://doi.org/10.1016/j.jastp.2014.07.003

Yue, J., Vadas, S. L., She, C. Y., Nakamura, T., Reising, S. C., Liu, H. L., & Li, T. (2009). Concentric gravity waves in the mesosphere generated by deep convective plumes in the lower atmosphere near Fort Collins, Colorado. *Journal of Geophysical Research*, *114*, D06104. https://doi.org/10.1029/2008JD011244

Zettergren, M. D., & Snively, J. B. (2013). Ionospheric signatures of acoustic waves generated by transient tropospheric forcing. *Geophysical Research Letters*, *40*, 5345–5349. https://doi.org/10.1002/2013GL058018

Zettergren, M. D., & Snively, J. B. (2015). Ionospheric response to infrasonic-acoustic waves generated by natural hazard events. *Journal of Geophysical Research: Space Physics*, *120*, 8002–8024. https://doi.org/10.1002/2015JA021116